Effect of Cr on Phase Transformation Behavior of Austenite in Fe-20Mn-9Al-1.2C-xCr Low-Density Steels During Isothermal Aging

Jianlei Zhang, Yueshan Jiang, Conghui Hu, Gang Ji, Changjiang Song, Qijie Zhai

Effect of Cr on Phase Transformation Behavior of Austenite in Fe-20Mn-9Al-1.2C-xCr Low-Density Steels During Isothermal Aging

Jianlei Zhang[1,2,3] · Yueshan Jiang[2] · Conghui Hu[1,2] · Gang Ji[3] · Changjiang Song[1,2] · Qijie Zhai[1]

Abstract
The influence of Cr on the microstructural evolution of austenite in Fe-20Mn-9Al-1.2C-xCr (wt%, x = 0, 3 and 6) low-density steels during isothermal aging at 650 °C for various durations was systematically investigated. With the isothermal aging processed, the 0Cr and 3Cr samples underwent the divorced eutectoid transformation followed by the eutectoid transformation, while only the eutectoid transformation was observed in the 6Cr sample. Meanwhile, increasing Cr content changed the eutectoid transformation products from ferrite + κ-carbide in the 0Cr sample to ferrite + κ-carbide + $M_{23}C_6$ carbide in the 3Cr sample, and to ferrite + M_7C_3 carbide in the 6Cr sample. The Cr addition significantly increased the A1 temperature (655 °C) of the 0Cr sample to 712 °C of the 3Cr sample, and to 841 °C of the 6Cr sample. As a result, the temperature difference between the A1 temperature and experimental phase transformation temperature (650 °C) was enlarged, which provided a greater driving force for the eutectoid transformation and accelerated the transformation rate of eutectoid transformation. In addition, the Cr addition had a significant effect on the diffusion of constituent elements, decreased the interlayer spacing of pearlite structure from 625 ± 30 nm in the 0Cr sample to 385 ± 25 nm in the 3Cr sample, and to 150 ± 20 nm in the 6Cr sample, refining the eutectoid structure. These findings revealed the mechanism regarding the effect of Cr addition on the eutectoid transformation of austenite, offering valuable insights into the microstructure design of high-performance low-density steels.

Keywords Low-density steel · Cr addition · Eutectoid transformation · Isothermal aging

1 Introduction

Recent years, Fe–Mn-Al-C steels have been receiving widespread attention, due to their excellent mechanical properties and low density [1–8]. Especially, the austenite based steels with high Mn and Al contents have achieved high ultimate tensile strength (UTS) of 800–1500 MPa and total elongation (TE) of 30–80% [1]. As reported in [2], the high Mn content greatly stabilized the austenite structure. The addition of Al element not only significantly reduces the density of steels (1.3% density reduction per 1 wt% Al addition) [1, 9], but also promotes the precipitation of κ-carbides favorable for yield strength increasement. In addition, these kinds of steels have an outstanding strain-hardening behavior due to the dislocation planar slip and corresponding characteristic dislocation substructures [10]. Therefore, the Fe-Mn-Al-C steels have great application prospects in many fields, including aircraft, chemical and automotive industries, etc. [1].

The excellent mechanical properties of austenite based steel are closely related to the constituent phase and microstructure evolution. Austenite plays a vital role on the performance of steels, not only because of its own excellent properties, but also because of its rich phase transformation pathways [11]. The common austenite decomposition reactions include: discontinuous precipitation, precipitation

✉ Gang Ji
gang.ji@univ-lille.fr

✉ Changjiang Song
riversong@shu.edu.cn

[1] Center for Advanced Solidification Technology (CAST), School of Materials Science and Engineering, Shanghai University, Shanghai 200444, China

[2] State Key Laboratory of Advanced Special Steel, School of Materials Science and Engineering, Shanghai University, Shanghai 200444, China

[3] UMR 8207-UMET-Unité Matériaux et Transformations, Univ. Lille, CNRS, INRAE, Centrale Lille, 59000 Lille, France

transformation, cellular transformation and spinodal decomposition [11]. Nanoscale intragranular κ-carbide could directly form in austenite by spinodal decomposition or nucleation-growth mechanisms [1, 12], which could significantly improve strength and maintain good elongation [13–15]. A lamellar discontinuous precipitation (ferrite + κ-carbide) was observed along austenite grain boundaries in a Fe-27Mn -8.5Al-1.0Si-0.92C (wt%) steel after aging at the temperatures ranging from 627 to 777 °C [16]. W.C. Cheng et al. [17] have found that a microstructure containing ferrite, κ-carbide and $M_{23}C_6$ carbide formed by a eutectoid reaction of austenite in a Fe-13.5Mn-6.3Al-0.78C (wt%) steel below 650 °C. A cellular transformation of austenite → austenite + ferrite + κ-carbide occurred in a Fe-17.9Mn-7.1Al-0.85C (wt%) austenitic steel at temperatures below 775 °C [18]. Therefore, understanding the different phase transformation behaviors of austenite would be potential for obtaining excellent mechanical properties of low-density steel.

The addition of Cr in the low-density steels has been expected to obtain excellent comprehensive mechanical properties with high strength and good plasticity [15, 19, 20]. On the one hand, the Cr addition was found to suppress the precipitation and growth of intragranular κ-carbide in austenite, which decreased the yield strength [15, 21]. At the same time, the Cr addition has been proved to suppress the formation of coarse κ-carbides along grain boundaries favoring good plasticity [22] and promote the formation of DO3 phase in austenite [22, 23]. On the other hand, some Cr-bearing carbides, such as $Cr_{23}C_6$ and Cr_7C_3, were observed in austenite of a Fe-8.7Al-28.3Mn-1C-5.5Cr (wt%) steel after aging treatment in a board temperature range [24]. Our previous work [21] has found that the $Cr_{23}C_6$ carbides could precipitate in Fe-28Mn-9Al-1.2C-9Cr (wt%) low-density steel, and significantly increased the tensile strength of the steel. In addition, K.W. Kim et al. [22] found that as Cr content exceeded 5 wt% in Fe-20Mn-12Al-1.5C (wt%) steel, the M_7C_3 carbides precipitated in austenite and increased tensile strength while decreased the elongation. In addition, Cr was also found to increase the driving force for the transformation of austenite to ferrite in a medium-carbon low-alloy steel [25]. However, the effects of Cr addition on the transformation behavior of austenite in low-density steel during isothermal aging is still unclear. This provides a barrier to understand how to control the strengthening phase precipitation and phase transformation in austenite by Cr addition.

Therefore, in this work, the effects of Cr addition on the austenite transformation mechanism during isothermal aging were investigated in the Fe-20Mn-9Al-1.2C-xCr (wt%; x = 0, 3 and 6) steels. For the purpose, the low-density steels underwent aging treatment at 650 ˚C for various durations, because this temperature has been proven to be a suitable temperature for the multiphase transformation of austenite [17, 26]. The studied steel strips were prepared by near-net shape method under near-rapid solidification. Previous works [15, 27] have found that this simple method could directly prepare thin steel strips with a thickness of several millimeters without additional rolling process, and the microstructure and mechanical properties of these steels were comparable with those prepared by the conventional preparation method, as referred in [28]. The austenite transformation was then systematically investigated using X-ray diffraction (XRD), scanning (SEM) and transmission electron microscopy (TEM). The experimental results were discussed with the aid of thermodynamic calculations.

2 Experimental

The Fe-20Mn-9Al-1.2C-xCr (wt%; x = 0, 3 and 6) low-density steels, hereafter shortly named to 0Cr, 3Cr and 6Cr samples respectively, were prepared by centrifugal casting under near-rapid solidification in an argon atmosphere. The detailed processes can be referred to our previous works [15, 27]. The metal ingots were melted by induction melting, and the molten metal was poured into a copper mold rotating at 600 rpm to obtain the steel strips with the size of 80 mm × 60 mm × 2.5 mm. Subsequently, the as-cast steel samples with different Cr contents were aged at 650 °C for various durations (0.5 h, 1 h, 3 h, 6 h, 9 h and 12 h) to investigate the microstructure evolution of austenite.

The composition of the steel samples was measured by using inductively coupled plasma mass spectrometry and a CS2800 carbon–sulfur analyzer. The measured compositions are shown in Table 1. The phase analysis was performed by an X-ray Diffractometer (Rigaku, D/Max-2200, Cu target operated at 40 kV and 40 mA), in which the wavelength of radiation was λ = 0.154056 nm and the scanning angle was 30 − 100°, scanning mode was continuous scanning with a speed of 4°/min. The microstructures were investigated by a scanning electron microscope (SEM, JSM-7800F FEG-SEM) equipped with an electron backscattered diffraction (EBSD) and an energy dispersive X-ray analysis (EDX) detectors. The SEM samples were wet ground to 4000 grit and subsequently electro-polished in a solution of 10 vol% perchloric acid and 90 vol% ethanol. TEM examination of precipitates was carried out using a FEI Tecnai G2-20 twin

Table 1 Measured compositions of the studied low-density samples (wt%)

Samples	Mn	Al	C	Cr	Fe
0Cr	19.87	8.79	1.17	–	Bal.
3Cr	19.95	8.92	1.15	3.05	Bal.
6Cr	19.90	8.95	1.16	6.00	Bal.

microscope, operated at 200 kV. TEM samples of 3 mm in diameter were prepared by a Struers TenuPol-5 twin-jet electro polisher operated at around 8 °C and 25 V, using a solution consisting of 5% perchloric acid and 95% acetic acid.

3 Results

Figure 1 shows the equilibrium phase diagram of Fe-20Mn-9Al-1.2C-xCr (wt%, x = 0–7) low-density steels, which was calculated by Thermo-Calc. (TCFE 9.0 database). According to Fig. 1(a), with increasing the Cr content, the equilibrium structures of the samples at 650 °C can be changed from α-ferrite + κ-carbide to α-ferrite + κ-carbide + M_7C_3 carbide, then to α-ferrite + M_7C_3 carbide. The addition of Cr promotes the precipitation of M_7C_3 carbide, while suppresses the formation of κ-carbide. In addition, the Cr addition increases the A1 temperature of the low-density steels significantly. According to the calculated equilibrium phase fraction diagram of the 0Cr, 3Cr and 6Cr samples shown in Fig. 1(b–d), the A1 temperatures of the 0Cr, 3Cr and 6Cr samples are 655 °C, 712 °C and 841 °C, respectively. Therefore, the transformation pathways, austenite → ferrite + κ-carbide, austenite → ferrite + κ-carbide + M_7C_3 carbide and austenite → ferrite + M_7C_3 carbide, are expected in the 0Cr, 3Cr and 6Cr samples during isothermal aging at 650 °C, respectively.

According to the XRD patterns shown in Fig. 2, the as-cast 0Cr, 3Cr and 6Cr samples are all consist of austenite and ferrite. As the aging begins, the diffraction peaks of the κ-carbides appear in the 0Cr and 3Cr samples after the aging for 0.5 h, and the volume fraction of ferrite increases significantly, as shown in Fig. 2(a) and (b). However, almost all the austenite in the 6Cr sample is transformed into ferrite after the aging for 0.5 h, and no diffraction peak of κ-carbide is found, as shown in Fig. 2(c). With the extension of the aging time, the volume fraction of ferrite and κ-carbide further increases in the 0Cr and 3Cr samples, while that of austenite gradually decreases. After the aging for 12 h, the constituent phases of the 0Cr sample are ferrite, austenite and κ-carbide. But the diffraction peak of the austenite disappears in the 3Cr sample after the aging for 9 h, only the ferrite and κ-carbide are remained. And the volume fraction of κ-carbides in the 3Cr sample is lower than that in the 0Cr sample. In the 6Cr sample,

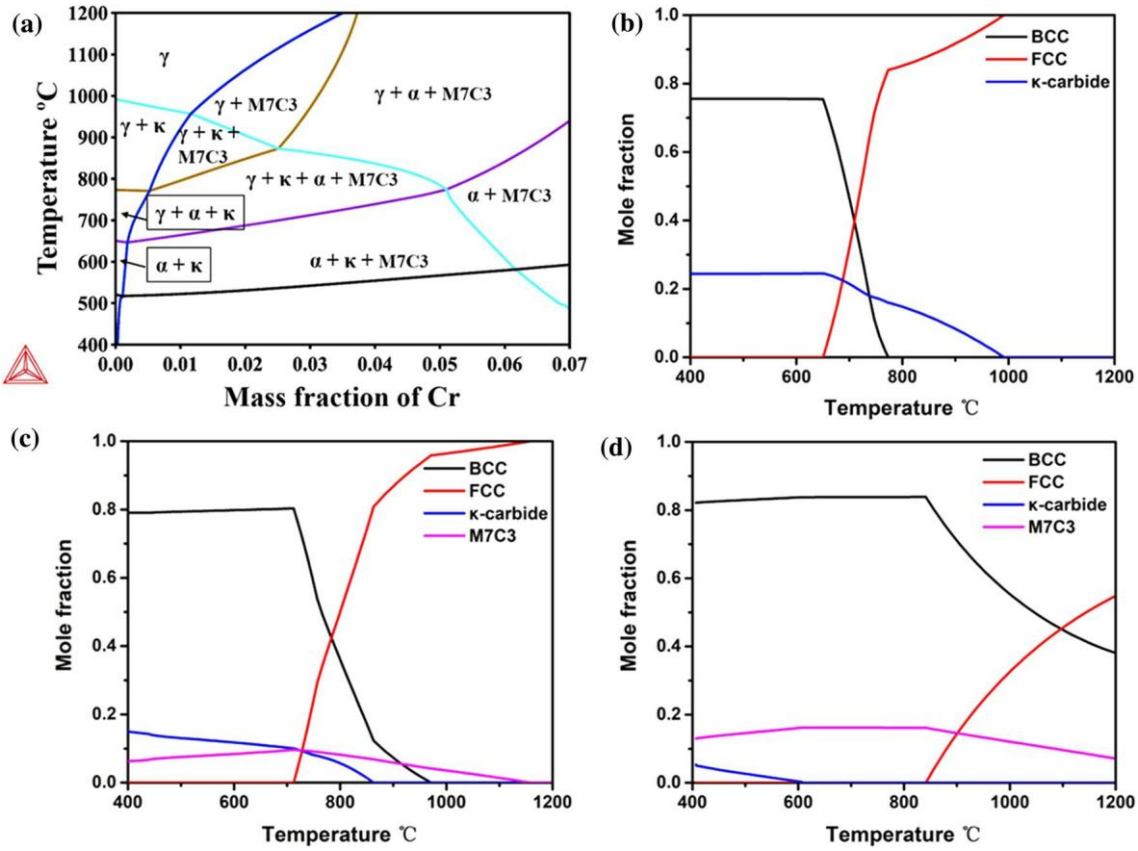

Fig. 1 **a** Thermodynamic equilibrium phase diagram of Fe-20Mn-9Al-1.2C-(0–7)Cr samples; **b–d** are the calculated equilibrium phase fraction in the 0Cr, 3Cr and 6Cr samples, respectively

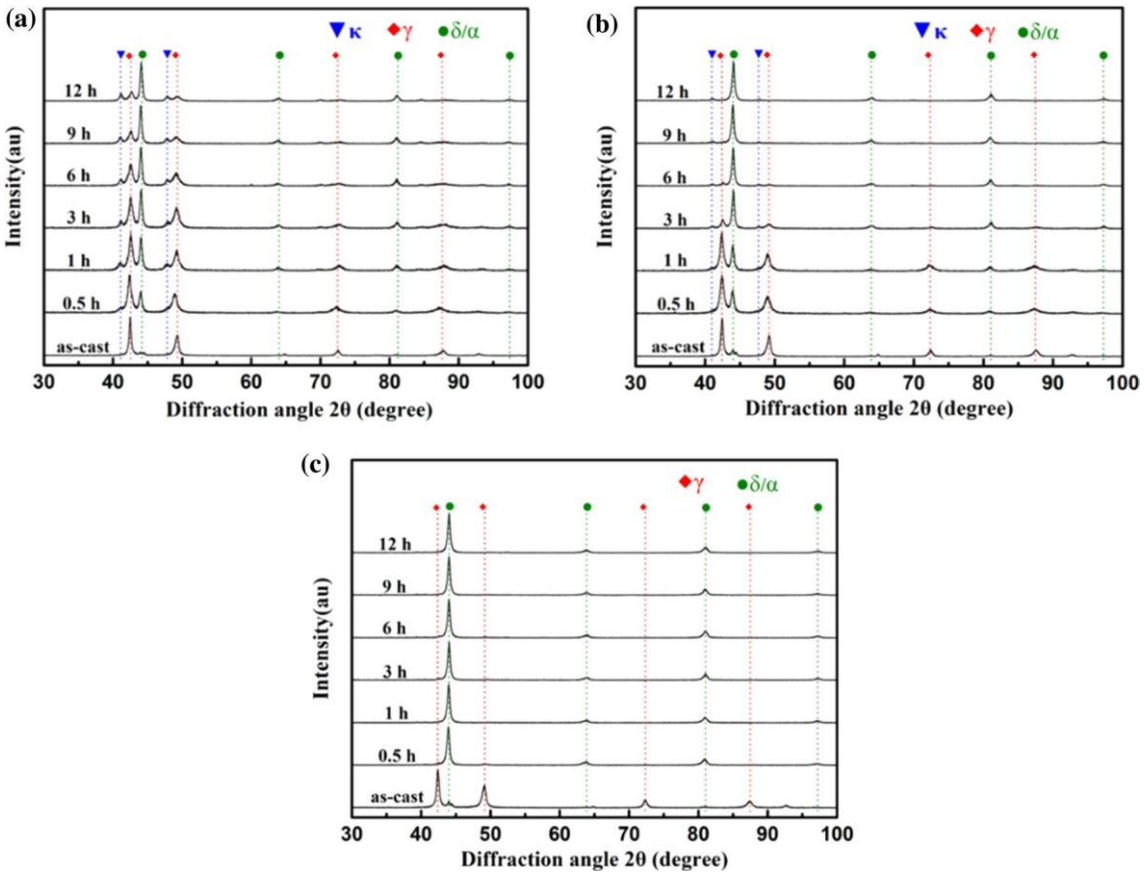

Fig. 2 XRD patterns of the samples aged at 650 °C for the various durations: **a** 0Cr, **b** 3Cr and **c** 6Cr samples

only the diffraction peaks of ferrite are visible during the subsequent long-term aging treatment.

Figure 3(a–c) show the island-like δ-ferrite distributed in the austenite matrix of all the as-cast 0Cr, 3Cr and 6Cr samples, respectively. According to our previous work [15], the volume fractions of δ-ferrite in the as-cast 0Cr, 3Cr and 6Cr samples are 3%, 12% and 18%, respectively. Due to the cube-on-cube orientation relationship between κ-carbide and γ-austenite of $[100]_\kappa$ // $[100]_\gamma$ and $(001)_\kappa$ // $(001)_\gamma$ [1], the TEM dark-field (DF) micrographs using (001) superlattice reflections show a lot of κ-carbide precipitates in the austenite of these samples, as shown in Fig. 3(d–f). The size and

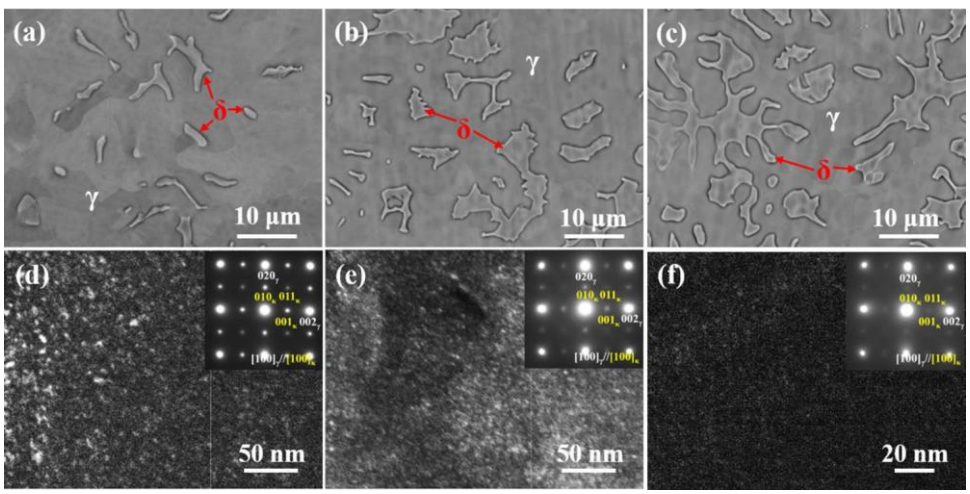

Fig. 3 SEM and TEM micrographs of the as-cast 0Cr, 3Cr and 6Cr samples: **a–c** are the SEM micrographs of the as-cast 0Cr, 3Cr and 6Cr samples, respectively; **d-f** are the TEM DF micrographs of κ-carbides in austenite of the as-cast 0Cr, 3Cr and 6Cr samples, respectively. Insets in **d-f** are corresponding selected area electron diffraction patterns (SADPs)

volume fraction of the κ-carbide precipitates are decreased by increasing Cr content.

Figure 4 shows the microstructures of the 0Cr sample after the aging at 650 °C for 0.5 h. After the aging, the ferrite grows into the austenite with needle-like protrusions, and some spherical precipitates with a size of tens to hundreds of nanometers (as indicated by C1 in Fig. 4b) form along with the transformation of austenite → ferrite, as shown in Fig. 4(a–c). According to the nanobeam diffraction (NBD) pattern taken from the spherical precipitates in ferrite along with [211] zone axis (Fig. 4d), the spherical precipitates are proved to be κ-carbides [29]. Therefore, a transformation of austenite → ferrite + spherical κ-carbide is observed here, the transformation product is not the conventional lamellar pearlite but spherical κ-carbides and ferrite. In addition, no obvious orientation relationship between carbide and ferrite is detected by electron diffraction using TEM. Therefore, it can be inferred that this transformation is a divorced eutectoid transformation [30, 31]. In addition, the superlattice reflections in the SADP along $[110]_{\alpha}$ (Fig. 4 e) indicate that so many ordered DO3 phases are precipitated in the ferrite [15]. Different from the spherical κ-carbides in ferrite (Fig. 4c), the nano-scaled intragranular κ-carbide in austenite is increased in the volume fraction and size (~ 10 nm) after aging, as shown in Fig. 4(f).

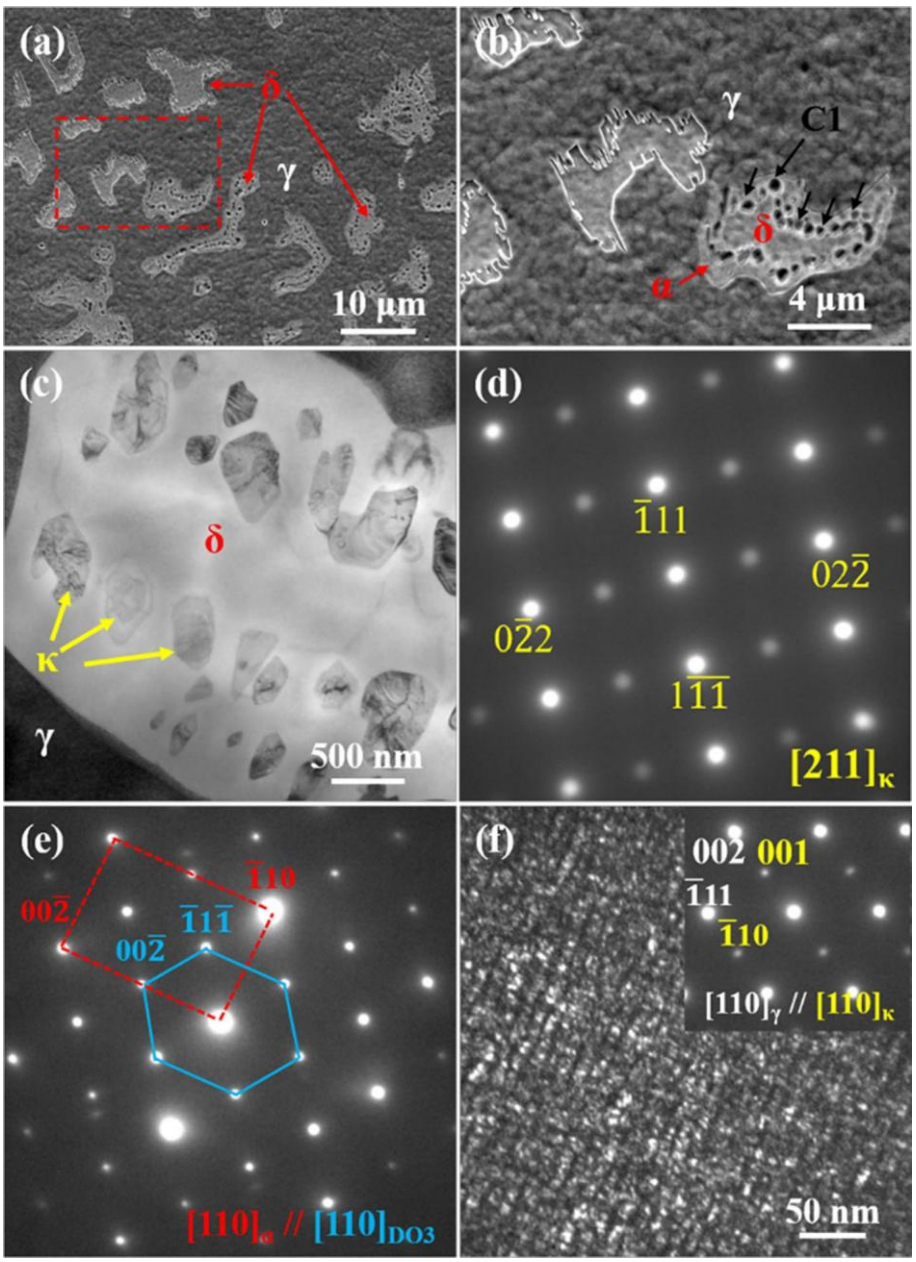

Fig. 4 Microstructure analysis of the 0Cr sample after the aging at 650 °C for 0.5 h: **a** and **b** are the SEM micrographs; **b** is the magnified SEM micrograph from the rectangular region indicated by red dotted line in **a**; **c** is TEM bright-field (BF) micrograph of ferrite; **d** is the NBD pattern taken from the spherical precipitates in ferrite along with [211] zone axis; **e** is the SADP taken from ferrite along with [110]α zone axis; **f** is the TEM DF micrograph of the κ-carbides in austenite and the inset is the corresponding SADP pattern

The microstructures of the 3Cr sample after the aging at 650 °C for 0.5 h are shown in Fig. 5. A similar divorced eutectoid transformation is also observed in the 3Cr sample, as shown in Fig. 5(a–b). Besides the spherical precipitates, there are some irregular precipitates produced during the phase transformation, as shown in Fig. 5(c). The spherical precipitates in ferrite are proved to be κ-carbides by SADP, as shown in Fig. 5(d), while the irregularly shaped precipitates are proved to be $M_{23}C_6$ carbides by NBD along with [1 $\bar{1}$2] zone axis [32], as shown in Fig. 5(e). Therefore, the phase transformation of the 3Cr sample can be described as austenite → ferrite + κ-carbide + $M_{23}C_6$ carbide after the isothermal aging. And the average size of κ-carbide precipitates in austenite is increased to ~ 8 nm in the 3Cr sample, as shown in Fig. 5(f).

Figure 6 shows the microstructures of the 6Cr sample after the aging at 650 °C for 0.5 h. A large amount of pearlite is observed, and some retained austenite and δ-ferrite are present, as shown in Fig. 6(a–b). According to Fig. 6(c), many precipitates are present in the pearlite structure where some precipitates (C2) are irregular-shaped, the others (C3) are elongated. In order to determine the C2 and C3 precipitates, NBD is performed to the two precipitates, as shown in Fig. 6(d) and (e). The NBD patterns along with [11 $\bar{2}$ 0] and [10 $\bar{1}$1] prove that both the precipitates belong to M_7C_3 carbides [32, 33]. According to the microstructure shown in

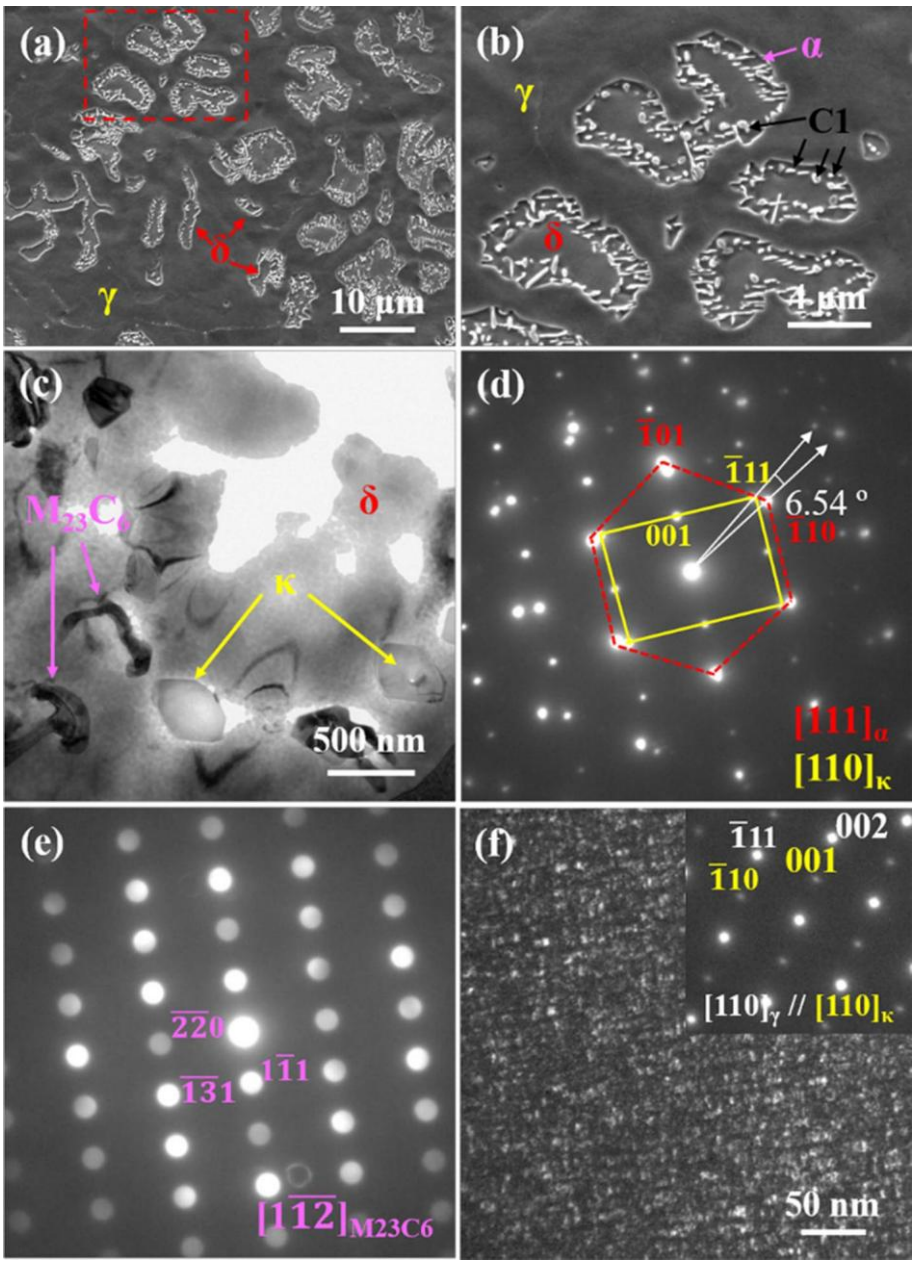

Fig. 5 Microstructure analysis of the 3Cr sample after the aging at 650 °C for 0.5 h: **a** and **b** are the SEM micrographs; **b** is the magnified SEM micrograph from the rectangular region indicated by red dotted line in **a**; **c** is TEM BF micrograph of ferrite; **d** is the SADP taken from the ferrite and spherical precipitates along with [111]α zone axis; **e** is the NBD taken from irregularly shaped precipitates along with [1 (12)$\bar{}$] zone axis; **f** is the TEM DF micrograph of the κ-carbides in the austenite and the inset is the corresponding SADP pattern

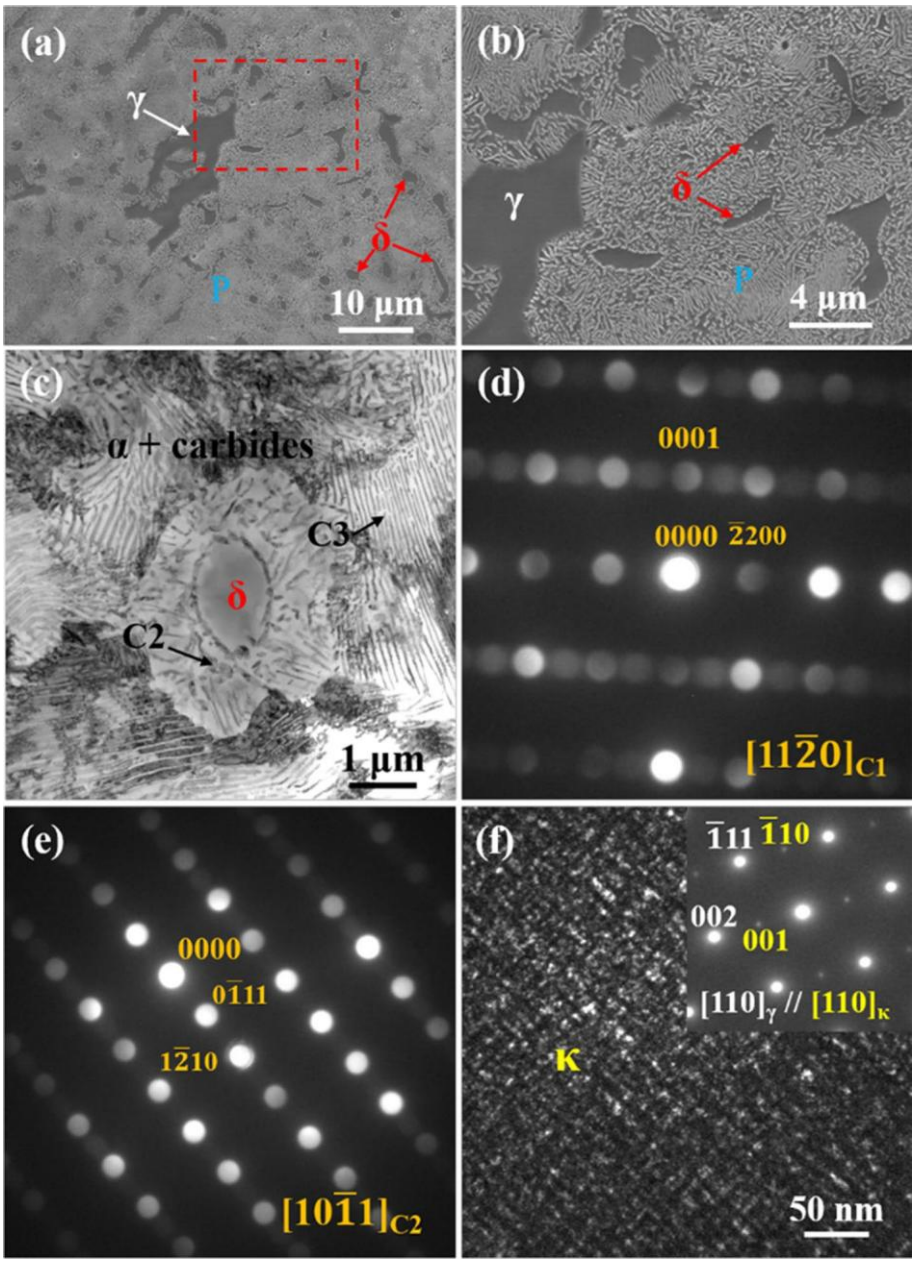

Fig. 6 Microstructure analysis of the 6Cr sample after the aging at 650 °C for 0.5 h: **a** and **b** are the SEM micrographs; **b** is the magnified micrograph from the rectangular region indicated by red dotted line in **a**; **c** is TEM BF micrograph of ferrite in the 6Cr sample; **d** is the NBD taken from the C2 precipitates along with [11 2^{-}0] zone axis; **e** is the NBD taken from the C3 precipitates along with [10 1^{-}1] zone axis; **f** is the TEM DF micrograph of the κ-carbides in the austenite and the inset is the corresponding SADP pattern

Fig. 6(c), it can be inferred that a eutectoid transformation of austenite → ferrite + M_7C_3 carbide takes place. In addition, no κ-carbide is observed during this transformation, but the average size of κ-carbides in the retained austenite is increased to ~ 6 nm, as shown in Fig. 6(f). However, although a large number of carbides appear in SEM and TEM micrographs, the diffraction peak of carbides is not observed in the XRD patterns, as shown in Fig. 2(c). This may be due to the too large difference in intensity of the diffraction peaks between ferrite matrix and carbides, making it difficult to be observed clearly in the normalized XRD patterns.

After the aging at 650 °C for 3 h, some lamellar pearlite structures form by eutectoid transformation of austenite surrounding the divorced eutectoid structures in the 0Cr sample, as shown in Fig. 7(a) and (b). The lamellar carbides in this structure are determined as κ-carbides, as shown in Fig. 7(c). The average size of intragranular κ-carbide in austenite is significantly increased to ~ 15 nm, as shown in Fig. 7(d). Similarly, a eutectoid transformation is also observed in the austenite of the 3Cr sample, as shown in Fig. 8. And the transformation products are the same as the previous divorced eutectoid transformation, i.e. ferrite + κ-carbide + $M_{23}C_6$ carbide. Compared with the 0Cr sample, more austenite in the 3Cr sample is decomposed by eutectoid transformation. The average size of intragranular κ-carbide in the 3Cr is increased to ~ 13 nm,

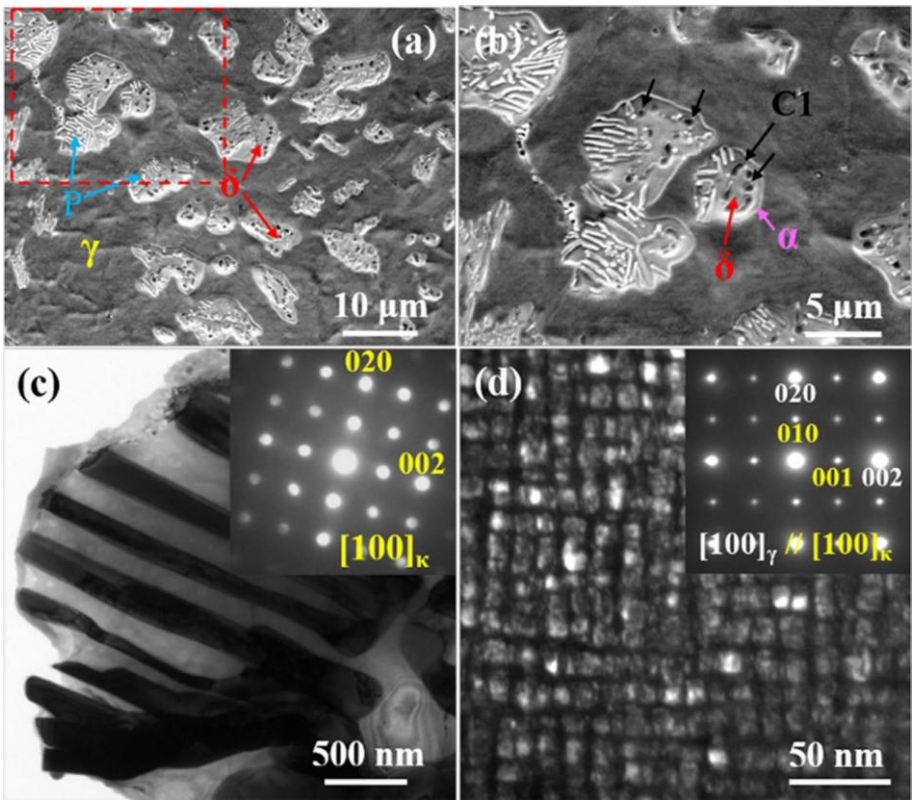

Fig. 7 Microstructure analysis of the 0Cr sample after the aging at 650 °C for 3 h: **a** and **b** are the SEM micrographs; **b** is the magnified micrograph from the rectangular region indicated by red line in **a**; **c** is TEM BF micrograph of ferrite in the 0Cr sample; **d** is the TEM DF micrograph of the κ-carbides in the austenite

which is still smaller than that in the 0Cr sample. Further, the microstructure of the 6Cr sample is mainly lamellar pearlite structures and retained δ-ferrite, and the austenite is almost completely decomposed, as shown in Fig. 9. The lamellar pearlite structure consists of ferrite + M_7C_3 carbides, no new transformation product is observed.

After the aging at 650 °C for 9 h, the eutectoid transformation continues to advance around the divorced eutectoid structure in the 0Cr sample, as shown in Fig. 10(a) and (b). However, the austenite is almost completely decomposed by eutectoid transformation in the 3Cr sample, only the lamellar pearlite structures and retained δ-ferrite are present just like that in the 6Cr sample, as shown Fig. 10(e–f). The difference of microstructure between the 3Cr and 6Cr samples is that the pearlite structures in the 3Cr sample consist of κ-carbides + $M_{23}C_6$ carbides + ferrite, while M_7C_3 carbides + ferrite in the 6Cr sample. Therefore, it can be concluded that with extension of the aging time, the eutectoid transformation becomes dominant while divorced eutectoid transformation only takes place surrounding the original δ-ferrite at the first transformation stage. It should be noted that the interlayer spacing of pearlite structure is decreased with increasing Cr content at this aging stage. The interlayer spacing of pearlite structure in the 0Cr, 3Cr and 6Cr samples after the aging for 9 h is measured as about 625 ± 30 nm, 385 ± 25 nm and 150 ± 20 nm, respectively. This indicates that the addition of Cr can refine the pearlite structure significantly.

4 Discussion

As shown above, the aging treatment at 650 °C causes the 0Cr and 3Cr samples to first undergo a divorced eutectoid transformation at the phase boundary between δ-ferrite and austenite. With the extension of aging time, the eutectoid transformation begins to take place around the divorced eutectoid structure, and finally the austenite is completely transformed into the pearlite structure. However, only eutectoid transformation is observed in the 6Cr sample. The phase transformation sequence in the 0Cr and 3Cr samples is summarized schematically, as shown in Fig. 11. The as-cast low-density samples consist of austenite and a small amount of δ-ferrite, as shown in Fig. 3. As the aging progresses, a transformation of austenite → ferrite occurs at the phase boundary between austenite and δ-ferrite. The ferrite continuously grows toward austenite at the phase boundary in the form of needle-like protrusions. At the same time, some spherical or irregularly shaped carbides (in the 3Cr sample) form at the phase boundary with the growth of ferrite by divorced eutectoid transformation. After the divorced

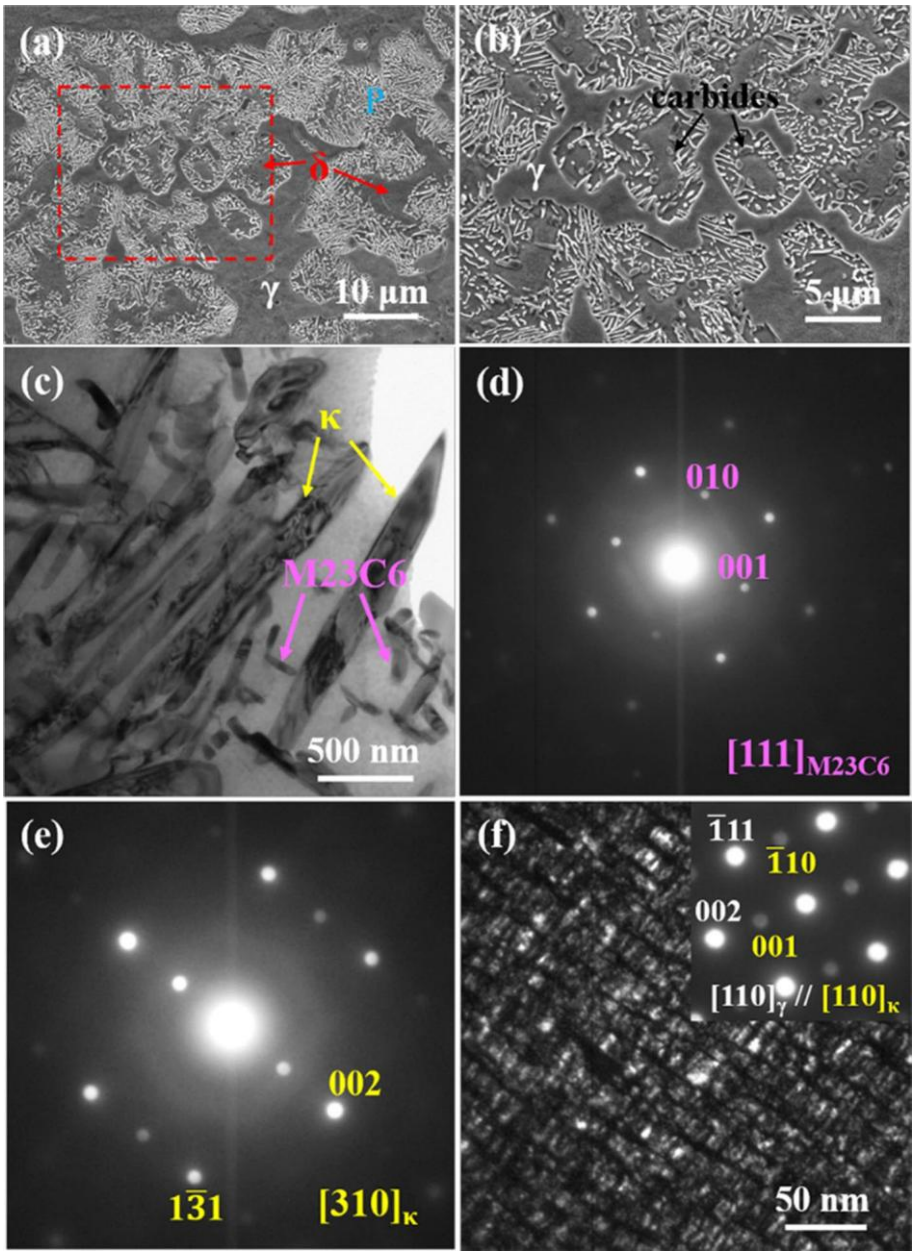

Fig. 8 Microstructure analysis of the 3Cr sample after the aging at 650 °C for 3 h: **a** and **b** are the SEM micrographs; **b** is the magnified micrograph from the rectangular region indicated by red dotted line in **a**; **c** is TEM BF micrograph of ferrite in the 3Cr sample; **d** is the SADP taken from the irregularly shaped M23C6 carbides along with [111]M23C6 zone axis; **e** is the NBD taken from lamellar κ-carbide precipitates along with [310]κ zone axis; **f** is the TEM DF micrograph of the κ-carbides in the austenite and the inset is the corresponding SADP pattern

eutectoid transformation, the austenite gradually transforms into lamellar pearlite structure by eutectoid transformation.

It should be noted that the intragranular κ-carbides in austenite gradually increase in size with the extension of the aging time, and disappears after the austenite is completely decomposed. During the eutectoid reaction, the lamellae of carbide and ferrite progressively grow into austenite, the phase transform interface is shown in Fig. 12, as pointed by the white arrow. W.C. Cheng et al. [34] have found that in a Fe-17.9Mn-7.1Al-0.85C (wt%) sample, the intragranular κ-carbides in austenite could grow into large rafted precipitates, and then change to lamellar phase after prolonged aging. A similar phenomenon was also discovered by C. Mapelli et al. [11]. Therefore, it can be inferred that the nano-scale intragranular κ-carbides constantly coarsen and eventually become a lamellar structure during eutectoid reaction. W.K. Choo et al. [35] have also found that the pre-existing ordered κ-carbide particles in the matrix were converted to coarser lamellar κ-carbide at a grain boundary reaction front in a Fe-30Mn-7.8Al-1.3C (wt%) sample.

According to the results above, the phase transformation in the 0Cr sample can be concluded as austenite → ferrite + κ-carbide; while that in the 3Cr sample is austenite → ferrite + κ-carbide + $M_{23}C_6$ carbide; that in the 6Cr sample is austenite → ferrite + M_7C_3 carbide. The experimental results in the 0Cr and 6Cr samples are in good agreement with the results calculated by phase diagram (Fig. 1), while M_7C_3 carbides was not observed in

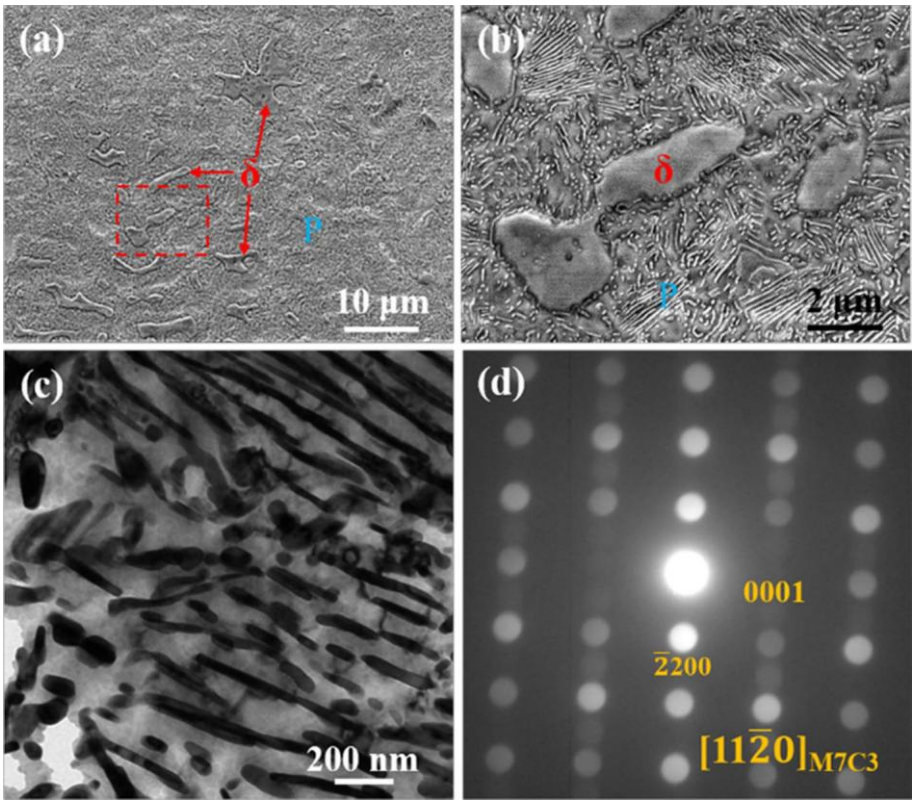

Fig. 9 Microstructure analysis of the 6Cr sample after the aging at 650 °C for 3 h: **a** and **b** are the SEM micrographs; **b** is the magnified micrograph from the rectangular region indicated by red dotted line in **a**; **c** is TEM BF micrograph of ferrite in the 6Cr sample; **d** is the NBD taken from the precipitates along with [1120] zone axis

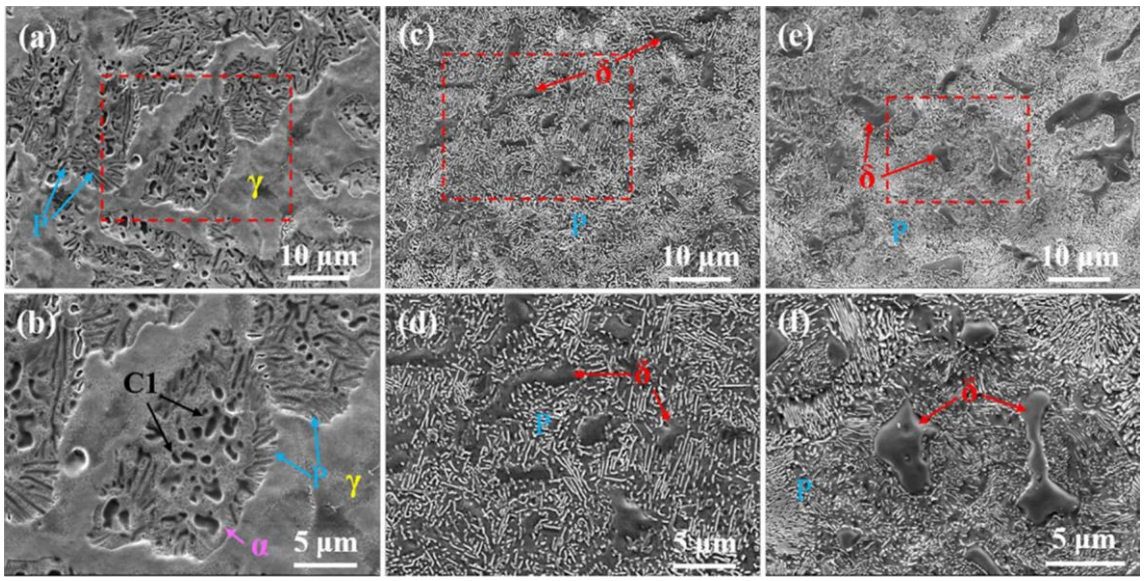

Fig. 10 SEM micrographs of the 0Cr **a, b**, 3Cr **c, d** and 6Cr **e, f** samples after the aging at 650 °C for 9 h, respectively; **b**, **d** and **f** are the magnified SEM micrographs from the rectangular regions indicated by red dotted line in **a**, **c** and **e**, respectively

the 3Cr sample and $M_{23}C_6$ carbides was present. Therefore, it can be inferred that the high Cr content has a high driving force for the formation of M_7C_3 carbides during eutectoid transformation and also inhibits the produc- tion of κ-carbides. However, the low Cr content is more conducive to the formation of $M_{23}C_6$ carbides in this eutectoid transformation.

In this work, a divorced eutectoid transformation takes place before the eutectoid transformation in the austenite, which is rarely reported in this kind of low-density steels.

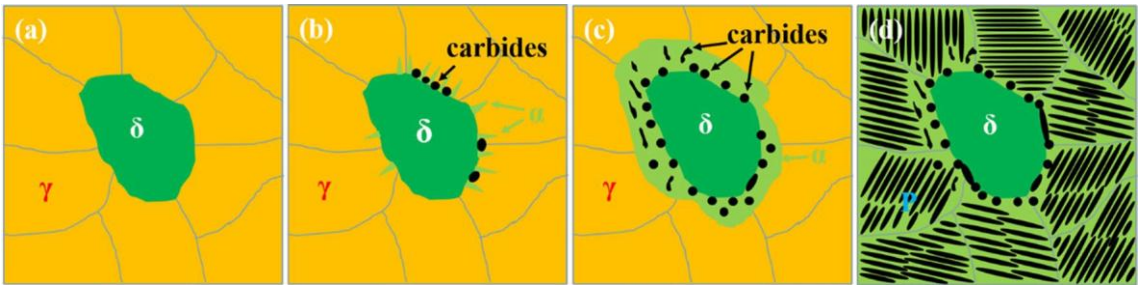

Fig. 11 Schematic illustration of the phase transformation sequence in the low-density samples during the ageing at 650 °C

Fig. 12 SEM micrographs of the 0Cr **a**, 3Cr **b** and 6Cr **c** samples after the aging at 650 °C for 3 h, respectively

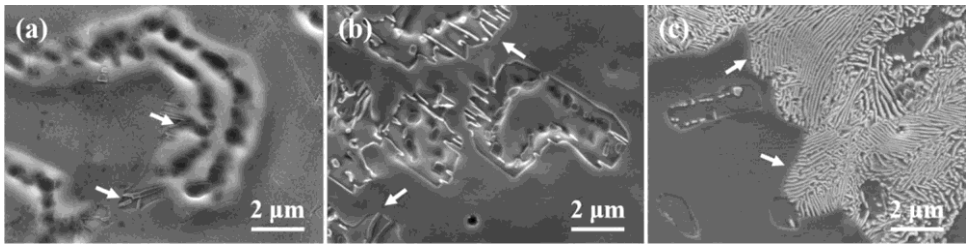

The conditions conducive to the occurrence of divorced eutectoid transformation are generally considered to be: a) the aging treatment temperature is close to and below A1 temperature; b) an austenite matrix containing arrays of fine and dense carbide particles; c) a lower undercooling [30, 31]. According to the calculated equilibrium phase fraction diagram of the 0Cr, 3Cr and 6Cr samples shown in Fig. 1(b–d), the used experimental transformation temperature of 650 °C is below the A1 temperatures of the 0Cr and 3Cr samples of around 655 °C and 712 °C, respectively. The smaller temperature difference between the transformation temperature and A1 temperature also leads to a smaller undercooling. Therefore, a divorced eutectoid transformation is observed in the 0Cr and 3Cr samples at the earlier transformation stage. As the phase transformation progresses, the composition of austenite in the 0Cr and 3Cr samples would change, and then the eutectoid transformation begins to occur. However, the A1 temperature of the 6Cr sample is calculated as 841 °C, which is much higher than the experimental transformation temperature (650 °C). The higher austenitizing temperature results in a greater tendency to form lamellar structure in the annealed sample [30]. As a result, only eutectoid structure is observed in the 6Cr sample aged at 650 °C for 0.5 h.

In addition, the increase in Cr content promotes the eutectoid transformation at 650 °C. As shown above, a large amount of austenite still exists in the 0Cr sample after the aging treatment at 650 °C for 12 h. However, the austenite in the 3Cr sample was completely transformed into the eutectoid structure by the aging treatment for 9 h. The austenite in the 6Cr sample is completely consumed within only 3 h. This can also be attributed to the increased A1 temperature of the samples caused by increasing the Cr content, as shown in Fig. 1. The enlarged difference between the A1 temperature and the transformation temperature (650 °C) provides a greater driving force for the eutectoid transformation and accelerates the phase transformation rate of the eutectoid transformation.

According to Fig. 10, the increase of Cr content decreases the interlayer spacing of pearlite, which could be affected by the element diffusion [36, 37] and undercooling. M. Honjo et al. [36] have found that the lamellar spacing of the pearlite structure in Fe-C-Cr samples was refined by increasing the Cr content, which was caused by a decrease of the diffusion coefficient of C in the austenite. The chemical composition of the original austenite in the as-cast samples and the pearlite structure after the aging for 9 h were measured by SEM–EDX, as shown in Table 2. In addition, the diffusion coefficients of different elements in austenite (FCC) at 650 °C were calculated by Thermo-Calc software with TCFE7 and MOBFE2 database, and the results are shown in Table 3. First, the Cr addition decreases the diffusion coefficient of C in austenite. Then, according to the element partition between the transformation products and the diffusion coefficient of different elements in austenite at 650 °C, Mn element is the limiting element affecting the phase transformation in the 0Cr sample, while Cr element is the limiting element in the 3Cr and 6Cr samples. The diffusion coefficient of Mn element of 8.1×10^{-19} $m^2 \cdot s^{-1}$ in the 0Cr sample is larger than those of Cr element of 1.76×10^{-19} $m^2 \cdot s^{-1}$ in the 3Cr sample and of 2.62×10^{-19} $m^2 \cdot s^{-1}$ in the 6Cr sample. It has been found that the faster the diffusion, the greater the interlayer spacing of pearlite [36]. Therefore, the interlayer spacing of pearlite in the 0Cr sample is the largest. However, although the diffusion coefficient of Cr

Table 2 The chemical composition of the different phase in the three samples (wt%)

Samples	Phases		Fe	Mn	Al	Cr
0Cr	γ		77.39 ± 0.22	15.31 ± 0.21	7.30 ± 0.16	–
	Pearlite	α	78.68 ± 0.56	10.86 ± 0.67	10.46 ± 0.21	–
		κ	62.11 ± 2.54	25.69 ± 2.45	12.20 ± 0.70	–
3Cr	γ		74.65 ± 0.11	15.32 ± 0.51	7.71 ± 0.54	2.32 ± 0.07
	Pearlite	α	75.26 ± 0.32	12.02 ± 0.49	10.84 ± 0.13	1.88 ± 0.13
		κ	55.78 ± 2.88	28.08 ± 2.64	11.75 ± 0.62	4.39 ± 0.42
		$M_{23}C_6$	42.45 ± 3.37	41.92 ± 5.35	3.12 ± 1.24	12.51±2.37
6Cr	γ		70.70 ± 0.21	15.29 ± 0.51	7.69 ± 0.54	6.32 ± 0.07
	Pearlite	α	72.64 ± 0.32	12.81 ± 0.49	10.66 ± 0.13	3.89 ± 0.13
		M_7C_3	41.73 ± 2.57	34.88 ± 2.54	2.94 ± 0.57	20.45±1.27

Table 3 The diffusion coefficient of different elements in the austenite (FCC)

Samples	Al/ $m^2 s^{-1}$	Mn/ $m^2 s^{-1}$	Cr/ $m^2 s^{-1}$	C/ $m^2 s^{-1}$
0Cr	4.23×10^{-18}	8.1×10^{-19}	–	3.34×10^{-13}
3Cr	4.8×10^{-18}	8.23×10^{-19}	1.76×10^{-19}	2.34×10^{-13}
6Cr	6.01×10^{-18}	9.44×10^{-19}	2.62×10^{-19}	1.2×10^{-13}

in the 6Cr sample is greater than that of the 3Cr sample, the interlayer spacing of pearlite in the 6Cr sample is still smaller than that of 3Cr sample. This should be attributed to the larger undercooling in the 6Cr sample resulting in a higher phase transformation rate, and the elements in the sample cannot diffuse sufficiently.

5 Conclusions

In this work, the effects of Cr on the microstructural evolution of austenite during isothermal aging at 650 °C in the austenitic-based Fe-20Mn-9Al-1.2C-xCr (wt%; x = 0, 3 and 6) low-density steels were investigated. The principal results obtained are summarized as follows:

(1) The addition of Cr changed the phase transformation mode of austenite in the samples during aging at 650 °C. The 0Cr and 3Cr samples underwent the divorced eutectoid transformation and then the eutectoid transformation. However, only the eutectoid transformation was observed in the 6Cr sample.
(2) The Cr addition had a significant effect on the transformation products of the eutectoid transformation at 650 °C in the three samples: 0Cr: austenite → ferrite + κ-carbide; 3Cr: austenite → ferrite + κ-carbide + $M_{23}C_6$ carbide; 6Cr: austenite → ferrite + M_7C_3 carbide.
(3) The increase of Cr content significantly increased the A1 temperature of the sample and corresponding difference between A1 temperature and aging temperature (650 °C), which promoted the eutectoid transformation.
(4) The addition of Cr content had a significant effect on the diffusion of elements, resulting in the refinement of the pearlite structure.

Acknowledgements Jianlei Zhang was grateful for his visiting Ph.D. project supported by the China Scholarship Council (Grant No. 201906890053). This work was financially supported by the National Natural Science Foundation of China (No. 51974184), National MCF Energy R&D Program of China (No. 2018YFE0306102). The electron microscopy facilities in Lille, France, is supported by the Conseil Regional du Nord-Pas de Calais and the European Regional Development Fund (ERDF).

Declarations

Conflict of interest The authors have no relevant financial or non-financial interests to disclose.

References

1. S.P. Chen, R. Rana, A. Haldar, R.K. Ray, Prog. Mater. Sci. **89**, 345–391 (2017). https://doi.org/10.1016/j.pmatsci.2017.05.002
2. O.A. Zambrano, J. Mater. Sci. **53**, 14003–14062 (2018). https://doi.org/10.1007/s10853-018-2551-6
3. Y. Kwon, J.H. Hwang, H.C. Choi, T.T.T. Trang, B. Kim, A. Zargaran, N.J. Kim, Met. Mater. Int. **26**, 75–82 (2020). https://doi.org/10.1007/s12540-019-00314-2
4. G. Park, S. Jeong, C. Lee, Met. Mater. Int. **27**, 2046–2058 (2021). https://doi.org/10.1007/s12540-020-00706-9
5. J. Moon, S.-J. Park, J.H. Jang, T.-H. Lee, C.-H. Lee, H.-U. Hong, H.N. Han, J. Lee, B.H. Lee, C. Lee, Acta Mater. **147**, 226–235 (2018). https://doi.org/10.1016/j.actamat.2018.01.051
6. M.J. Yao, E. Welsch, D. Ponge, S.M.H. Haghighat, S. Sandlöbes, P. Choi, M. Herbig, I. Bleskov, T. Hickel, M. Lipinska-Chwalek, P. Shanthraj, C. Scheu, S. Zaefferer, B. Gault, D. Raabe, Acta Mater. **140**, 258–273 (2017). https://doi.org/10.1016/j.actamat.2017.08.049
7. J. Moon, S.-J. Park, S.-D. Kim, J.H. Jang, T.-H. Lee, C.-H. Lee, B.H. Lee, H.-U. Hong, H.N. Han, J. Alloy. Compd. **804**, 511–520 (2019). https://doi.org/10.1016/j.jallcom.2019.06.362

8. C.W. Kim, M. Terner, J.H. Lee, H.U. Hong, J. Moon, S.J. Park, J.H. Jang, C.H. Lee, B.H. Lee, Y.J. Lee, J. Alloy. Compd. **775**, 554–564 (2019). https://doi.org/10.1016/j.jallcom.2018.10.104
9. G. Frommeyer, U. Brüx, Steel Res. Int. **77**, 627–633 (2006). https://doi.org/10.1002/srin.200606440
10. I. Gutierrez-Urrutia, ISIJ Int. **61**, 16–25 (2021). https://doi.org/10.2355/isijinternational.ISIJINT-2020-467
11. C. Mapelli, S. Barella, A. Gruttadauria, D. Mombelli, M. Bizzozero, X. Veys, J. Mater. Res. Technol. **9**, 4604–4616 (2020). https://doi.org/10.1016/j.jmrt.2020.02.088
12. J.L. Zhang, Y.S. Jiang, W.S. Zheng, Y.X. Liu, A. Addad, G. Ji, C.J. Song, Q.J. Zhai, Scripta Mater. **199**, 113836 (2021). https://doi.org/10.1016/j.scriptamat.2021.113836
13. W.W. Song, W. Zhang, J.V. Appen, R. Dronskowski, W. Bleck, Steel Res. Int. **86**, 1161–1169 (2015). https://doi.org/10.1002/srin.201400587
14. C. Haase, C. Zehnder, T. Ingendahl, A. Bikar, F. Tang, B. Hallstedt, W. Hu, W. Bleck, D.A. Molodov, Acta Mater. **122**, 332–343 (2017). https://doi.org/10.1016/j.actamat.2016.10.006
15. J.L. Zhang, C.H. Hu, Y.H. Zhang, J.H. Li, C.J. Song, Q.J. Zhai, Mater. Design **186**, 108307 (2020). https://doi.org/10.1016/j.matdes.2019.108307
16. S.-Y. Chang, L.-C. Tsao, T.-H. Chuang, S.-S. Wang, Metall. Mater. Trans. A **34**, 25–31 (2003). https://doi.org/10.1007/s11661-003-0205-y
17. W.-C. Cheng, Y.-S. Song, Y.-S. Lin, K.-F. Chen, P.C. Pistorius, Metall. Mater. Trans. A **45**, 1199–1216 (2014). https://doi.org/10.1007/s11661-013-2083-2
18. W.-C. Cheng, JOM **66**, 1809–1820 (2014). https://doi.org/10.1007/s11837-014-1088-7
19. Y. Sutou, N. Kamiya, R. Umino, I. Ohnuma, K. Ishida, ISIJ Int. **50**, 893–899 (2010). https://doi.org/10.2355/isijinternational.50.893
20. J. Moon, H.-Y. Ha, K.-W. Kim, S.-J. Park, T.-H. Lee, S.-D. Kim, J.H. Jang, H.-H. Jo, H.-U. Hong, B.H. Lee, Y.-J. Lee, C. Lee, D.-W. Suh, H.N. Han, D. Raabe, C.-H. Lee, Sci. Rep. **10**, 12140 (2020). https://doi.org/10.1038/s41598-020-69177-7
21. Y.X. Liu, M.X. Liu, J.L. Zhang, W. He, Z.P. Luo, C.J. Song, Q.J. Zhai, Mater. Sci. Eng. A **821**, 141583 (2021). https://doi.org/10.1016/j.msea.2021.141583
22. K.-W. Kim, S.-J. Park, J. Moon, J.H. Jang, H.-Y. Ha, T.-H. Lee, H.-U. Hong, B.H. Lee, H.N. Han, Y.-J. Lee, C.-H. Lee, S.-D. Kim, Mater. Charact. **170**, 110717 (2020). https://doi.org/10.1016/j.matchar.2020.110717
23. J.W. Lee, C.C. Wu, T.F. Liu, Scripta Mater. **50**, 1389–1393 (2004). https://doi.org/10.1016/j.scriptamat.2004.02.040
24. C.-F. Huang, K.-L. Ou, C.-S. Chen, C.-H. Wang, J. Alloy. Compd. **488**, 246–249 (2009). https://doi.org/10.1016/j.jallcom.2009.08.097
25. K. Chadha, D. Shahriari, C. Jr. Aranas, L.-P. Lapierre-Boire, M. Jahazi, Met. Mater. Int. **25**, 559–569 (2019). https://doi.org/10.1007/s12540-018-00227-6
26. W.-C. Cheng, S.-M. Hwang, Metall. Mater. Trans. A **42**, 1760–1766 (2011). https://doi.org/10.1007/s11661-010-0597-4
27. Y. Yang, J.L. Zhang, C.H. Hu, Z.P. Luo, Y.H. Zhang, C.J. Song, Q.J. Zhai, Mater. Sci. Eng. A **748**, 74–84 (2019). https://doi.org/10.1016/j.msea.2019.01.064
28. L.B. Liu, C.M. Li, Y. Yang, Z.P. Luo, C.J. Song, Q.J. Zhai, Mater. Sci. Eng. A **679**, 282–291 (2017). https://doi.org/10.1016/j.msea.2016.10.044
29. L. Sozańska Jędrasik, J. Mazurkiewicz, W. Borek, K. Matus, Arch. Metall. Mater **63**, 265–276 (2018). https://doi.org/10.24425/118937
30. J.D. Verhoeven, E.D. Gibson, Metall. Mater. Trans. A **29**, 1181–1189 (1998). https://doi.org/10.1007/s11661-998-0245-4
31. A.S. Pandit, H.K.D.H. Bhadeshia, Proc. R. Soc. A Math. Phys. **468**, 2767–2778 (2012). https://doi.org/10.1098/rspa.2012.0115
32. S.Q. Ma, J.D. Xing, Y.L. He, Y.F. Li, Z.F. Huang, G.Z. Liu, Q.J. Geng, Mater. Chem. Phys. **161**, 65–73 (2015). https://doi.org/10.1016/j.matchemphys.2015.05.008
33. Y.H. Tuan, C.L. Lin, C.G. Chao, T.F. Liu, Mater. Trans. **49**, 1589–1593 (2008). https://doi.org/10.2320/matertrans.MRA2008060
34. W.-C. Cheng, C.-Y. Cheng, C.-W. Hsu, D.E. Laughlin, Mater. Sci. Eng. A **642**, 128–135 (2015). https://doi.org/10.1016/j.msea.2015.06.096
35. W.K. Choo, J.H. Kim, J.C. Yoon, Acta Mater. **45**, 4877–4885 (1997). https://doi.org/10.1016/S1359-6454(97)00201-2
36. M. Honjo, T. Kimura, K. Hase, ISIJ Int. **56**, 161–167 (2016). https://doi.org/10.2355/isijinternational.ISIJINT-2015-395
37. J. Chance, N. Ridley, Metall. Trans. A **12**, 1205–1213 (1981). https://doi.org/10.1007/BF02642334